Al-Waaly, A. A.Y., Paul, M. C., and Dobson, P. (2017) Liquid cooling of non-uniform heat flux of a chip circuit by subchannels. *Applied Thermal Engineering*, 115, pp. 558-574. (doi:10.1016/j.applthermaleng.2016.12.061)

This is the author's final accepted version.

There may be differences between this version and the published version. You are advised to consult the publisher's version if you wish to cite from it.

http://eprints.gla.ac.uk/132789/

Deposited on: 13 December 2016

Enlighten – Research publications by members of the University of Glasgow
http://eprints.gla.ac.uk

Liquid Cooling of Non-Uniform Heat Flux of A Chip Circuit by Subchannels

Ahmed A. Y. Al-Waaly[123], Manosh C. Paul[1], Phillip Dobson[2]

[1]Systems, Power & Energy, [2]Electronics & Nanoscale Engineering, School of Engineering, University of Glasgow, G12 8QQ, UK
[3]Mechanical Engineering Department, College of Engineering, Wassit University, IRAQ
Email: Phil.Dobson@glasgow.ac.uk, Manosh.Paul@glasgow.ac.uk, aalwaaly@uowasit.edu.iq
Tel: +44(0)141 330 4314 (PD), +44(0)141 330 8466 (MP), +9647730888124(AH)

Abstract

Experimental and numerical analyses have been carried out to study the effect of using subchannels in a liquid cooled heat sink for minimising the effect of hotspots generated on a chip or circuit. Two heat sinks – with and without subchannels – were fabricated in order to investigate this effect. The first device was manufactured with normal parallel channels while the second was designed to extract more heat by dividing the main channels above the hotspot into two subchannels. The inlet and outlet manifolds were designed with two inlet ports to minimise any potential mal-distribution of mass flow rate through the channels. Three thermocouples were attached to the bottom surface of the inlet manifold and another three attached to the outlet manifold to record surface temperature. Five different mass flow rates were generated under gravity by changing water container height. The results show that adding subchannels improves the uniformity of temperature distribution and reduces the maximum temperature. Moreover, at the same pressure head 79cm the thermal resistance is reduced 20% whereas the pumping power is increased by 11%.

Keywords: Heat Transfer, Microchannels, Heat Sink, Microchannel fabrication, Numerical Simulation, Circuit cooling

1 Introduction

Parallel microchannels are the usual method for cooling high-density heat flux generated in a small-scale system [1]. However, using parallel microchannels in a cooling process generates a non-uniform temperature distribution because of mal-distribution of the mass flow rate through the microchannels, regardless of the uniformity of the heat generation of the chip itself [2]. Furthermore, Azizi et al.[3, 4] experimentally confirmed that uniform temperature distribution through the microchannels can be achieved if cylindrical heat sink was used.

Numerical results of Hegde et al.[5] confirm that the parallel fluid flow through a two-layer heat sink attached to a chip surface gives a lower surface temperature with decreasing heat flux generation. Their numerical results also showed that parallel flow with partial heating downstream gave a lower temperature compared to the counter flow case. This finding was consolidated by the experimental results of Wei [6].

Chauhan *et al.* [7] numerically investigated the effect of rearranging the chip layout. They studied three cases: first by placing high heat flux components at the inlets of the microchannels, second the flow was reversed and third counter flow was imposed between two adjacent microchannels. Their results confirmed that placing hotspots at the inlet resulted in improved cooling. Xie *et al.* [8] numerically analysed a combination of three different manifolds and two hotspot locations (in-line and diagonal arrangements perpendicular to the flow direction). They showed that a lower and more uniform temperature was achieved when the inlet and outlet ports were located at the middle and perpendicular to the heat sink surface, but a greater pressure was also produced. Analysis carried out by Biswal *et al.* [9] showed the effect of heat source size on thermal resistance, which was reduced by 16% for a fully developed flow and 14% for non-fully developed flow when the hotspot was moved from the inlet to the middle position with a heat source 25% the size of the heat sink.

Prasher and Chang [10] experimentally studied the effect of reducing channel widths above a hotspot with heat flux of 1250 W/cm^2. Their results demonstrated that a lower thermal resistance could be achieved by narrowing the channel above the hotspot. Numerical analysis of Minliang [11] and Wang [12] followed the same procedure i.e. narrowing the width of microchannels above the hotspot, to increase the fluid-solid interaction area. Their results showed that the chip temperature was reduced at the cost of an increased pressure drop. Zhang [13] et al. and Li et al. [14] divided a chip into low and high heat flux areas and also reduced the width of the microchannels above the hotspots to minimise the temperature with uniform heating. Their numerical results showed a good improvement in surface temperature.

The effect of channel width and wall thickness on minimising thermal resistance has been investigated by Türkakar and Özyurt [15]. A microchannel aspect ratio of 10 (height–to-width ratio), minimum wall thickness of 20µm and minimum channel width of 40 µm were considered as manufacturing constraints. Their optimum design confirmed that reducing microchannel width at the hot spot increases heat transfer but also increases the pressure drop.

Sharma et al. [16] used a special manifold design that enabled throttling of the flow above the heat flux locations, increasing mass flow over the hotspots. Two models were investigated, each with different heat flux generation: the first was 150 W/cm^2 and 20 W/cm^2, while the second was 300W/cm^2, 40W/cm^2 and 20 W/cm^2. The design proposed by the author showed an improvement in temperature uniformity by 4°C and 15°C for the first and second models respectively.

Dias [17] suggested a variable depth microchannel to reduce the high temperature at a hotspot. Above the hotspot, the channel was deeper than the surrounding background; this provided a larger area for the heat transfer interaction between fluid and solid. On the other hand, Goodson [18] suggested a complex manifold design that supplied a high flow rate to the hotspot, thereby reducing its temperature, while a reduced flow rate was provided to the background area. This was achieved supplying the cooling fluid directly to the hotspot through short, low resistance passages together with greater pumping power. Goodson used various microchannel sizes and fins of different heights to obtain a uniform temperature above the chip surface.

The effect of using oblique fins was investigated numerically by Lee [19] and experimentally by Lee [20]. Their analyses confirmed that the use of oblique fins led to a decrease in both the chip temperature and temperature difference above the chip surface. In addition, varying the fin density according to the heat dissipated at the hotspot improved temperature uniformity [20], but led to an increased pressure drop.

In the present study, the effect of using subchannels to enhance heat transfer from the hotspot generated on a chip circuit with non-uniform heat flux is investigated. The approach adopted employs an increase in the liquid-solid interaction area to remove the extra heat flux generated on the hotspot, therefore reducing the maximum surface temperature above the chip. Two heat sinks were fabricated: the first with parallel channels and the second with subchannels dividing the main channels into two above the hotspot. Inlet and outlet manifolds were designed with two ports in order to minimise any potential mal-distribution of mass flow rate through the channels. Consequently, the unique effect of the subchannels on heat sink performance has been investigated both theoretically and experimentally.

2 Experimental techniques

2.1 Test piece fabrication

Eleven channels were fabricated on a copper plate by CNC machining using a Datron CAT 3D-M6 with an accuracy of ±1μm. The properties of the copper are shown in Table 1. The dimensions of the cross-sectional area of the main channel(s) were 0.9mm×0.9mm while the subchannel dimensions were 0.3mm×0.9mm with a wall thickness of 0.3mm for both, see Fig. 1. The full dimensions for both models are shown in Fig. 2.

The lid was fabricated from polycarbonate [21] with two inlet and outlet ports, minimising potential mal-distribution of the mass flow rate through the channels as shown in Fig. 2. Epoxy with thermal conductivity of 0.2 [W/(m K)] (LOCTITE® 5145™ [22]) was used to join the copper plate and the lid together. Deionized water (DI) was fed to the models through two small stainless steel tubes which were inserted into the inlet holes. Moreover, outlet water flowed out of the model through the outlet stainless pipes (See Fig. 2). Transparent plastic tubes were used to provide and collect water to and from the model(s) (See [23] for the full tube specifications).

Twelve microheaters (Pt 6.8 M 1020 [24]) were used to generate both the uniform and hotspot heat fluxes. The nominal electrical resistance of each microheater was 6.8 Ohm at 0°C, allowing a maximum current of 2A within the working temperature range of -40°C to $+500^{o}$C. These microheaters were soldered to a PCB (See [25] for full specifications of this PCB). The full dimensions of a single microheater are also shown in Fig. 2.

Thermal paste [26] was used between the copper plate and the microheaters to improve thermal contact. The lid and the ceramic base were drilled with four holes each 2mm diameter in order to join all the parts with M2 screws (See Fig. 2). The base material was made from machinable ceramic [27].
Six type K thermocouples of size 200μm were each glued with epoxy to the bottom surface of the inlet and outlet manifolds at six positions enabling measurement of the temperature (See Fig. 2). A small drop of thermal paste [26] was added between the thermocouple probe and copper surface to improve heat transfer by minimising thermal resistance. The positions of each thermocouple are shown in Fig. 2.

The locations of the thermocouples were selected to be on the bottom surfaces of the inlet and outlet manifolds (see Fig. 2). Those locations were chosen in order to avoid passing thermocouple wires through a variable temperature medium and minimise the conduction error through the wires.

Another two type K thermocouples of size 200μm were inserted into the plastic tube close to the outlet ports enabling measurement of the water temperature. The thermocouple wires were pushed through the thermal insulation material to prevent any contact between the wires and the other surfaces (e.g. ceramics base), which could result in the possibility of conduction error through the wires [28]. The inlet water temperature was measured by immersing a thermocouple type K of size 200μm in the water container.

2.2 Experimental set-up

DI water was used as a working fluid and was supplied from a 7-liter water container with a large surface area (30cm×30cm). Different levels of the container were chosen to generate various flow rates under the action of gravity [29]. Two plastic tubes connected the container to the model inlet ports as shown in Fig. 3. The outer and inner diameter of the plastic tube were 3mm and 1.65mm respectively and the other specifications can be found in the Tygon® tubing documentation [23]. The device was wrapped with additional thermal insulation to minimise heat losses as shown in Fig. 3. Each set of H1 to H6 represents two microheaters, H1 & H4, H2 & H5, and H3 & H6 which were linked in series and supplied with a voltage from a single power supply (see Fig. 4). Background heat flux was generated by applying lower voltage to the micro-heater set H1 & H4 and H2 & H5, while a higher voltage is supplied to the set of H3&H6 to generate the hotspot at the middle position of the channels.

Thermocouple were connected to a laptop through a Pico data logger TC08 to record the temperatures. Water inlet temperature was measured with a type K thermocouple which was connected to a 2000T type K thermocouple thermometer manufactured by digitron [30]. One advantage of the TC08 is that it incorporates cold junction compensation, eliminating measurement variations caused by fluctuations in environmental temperature during the experiments.

Two power supplies were used to provide the required voltage: the first was a GPS-3303 series power supply with two channels of voltage range 0-30V, current 0-3A and accuracy of 0.01%+3mV manufacturing by GW Instek [31]. The second power supply was a single channel device model PL154 manufacturing by Thurlby Thandar Instruments with an accuracy of 0.1% for voltage and 0.3% for current [30] (See Fig.2 and Fig. 3). A digital balance was used to weigh the collected water during the experiments a shown in Fig. 3 and Fig. 4.

2.3 Thermocouple calibration

Thermocouple calibration was performed by comparing the thermocouple reading when fully submerged in crushed ice and boiling water with the standard water freezing and boiling temperature respectively [32]. A Pyrex beaker of two litres was filled with crushed ice and water, and the thermocouple probe was immersed for a sufficient length of time to avoid any effect of outside temperature on the reading. Additionally, during the calibration process a distance was left between the thermocouple probe and the bottom of the beaker to prevent the effect of heat transfer with the beaker base. Water freezing and boiling temperatures were considered (to 2 d.p.) to be those at standard atmospheric conditions (e.g. 1 atm) where water boils at 99.98^{o}C[1] and freezes at 0°C [34] .

2.4 Experimental methodology and steps

Experiments were performed inside a temperature controlled room for different pressure heads (25cm, 38cm, 47cm, 61cm, and 79cm). The following steps were followed during each run and for each pressure head:

1. The container was filled with filtered water to five millimetres above the required level. This took advantage of gravity to produce a stable, continuous flow rate **[29]**.
2. The (controlled) room temperature was allowed to stabilise (21°C).
3. The model and water were left to achieve thermal equilibrium for each part before starting each run of the experiment.
4. Each power supply was set to the desired voltage for each microheater to generate the required heat flux.
5. Thermocouple readings were monitored to ensure that steady-state had been achieved.
6. Thermocouple readings where then recorded for five minutes.
7. The water level was altered by changing the position of the container and steps 1-7 repeated for the next mass flow rate.

2.5 Experimental results and discussion

Experimental results were compared with the Reynolds number (*Re*) which was calculated based on the hydraulic diameter of the main channel of both models using:

$$Re=\frac{\rho\, U_m D_h}{\mu} \tag{1}$$

where U_m [m/s] represents the average inlet fluid velocity through the channel and D_h [m] is the hydraulic diameter of the main channel(s).
The heating power supplied by the microheaters was calculated from:

$$P=IV \tag{2}$$

Heat extracted from hotspot and background heat fluxes by the water was calculated from Eq.(3)

$$\dot{Q}=\dot{m}_w Cp_w (T_{wout}\text{-}T_{win}) \tag{3}$$

It was found that the maximum average heat loss was around 5% for each model.

[1]The boiling point of 99.98°C was used in accordance with the strict two-point calibration of Vienna Standard Mean Ocean Water (VSMOW) and as used elsewhere in the literature, see e.g. Roth and Friend [33] Chander Shekhar Sharma, N http://dx.doi.org/10.1016/j.apenergy.2014.10.068, [33] ibid.

Fig. 5(a) shows a comparison between the experimental readings of the thermocouples (*Thermocouple 1*, *Thermocouple 2* and *Thermocouple 3*) which were attached to the bottom surface of the outlet manifold for both the models with and without subchannels. The channels' width above the hotspot was reduced to one-third of that above the main channels (See section 2.1). Consequently, the solid-liquid interaction area increased, and the flow was accelerated at the entrance as a result of the contraction at the subchannels. Therefore, more energy was extracted from the hotspot by the water, leading to a drop in surface temperature. This reduction in temperature could be detected by the thermocouples attached on the bottom surface of the outlet manifold.

The hotspot had a negligible effect on the readings of thermocouples attached to the inlet manifold (See Fig. 5b). This is expected as the only effect this could have on the inlet thermocouple(s) was via conduction through the base of the inlet manifold.

Thermocouple 5 showed a lower temperature for the model with subchannels. The two inlet ports located at an equal distance from the mid-line of the inlet manifold (See Fig. 2 and Fig.6) caused more mixing at the middle position of manifold for the model with subchannels. Fig.6 shows the velocity distribution through the inlet manifolds for both models.

The other thermocouples (*Thermocouple 4* and *Thermocouple 6*) had approximately the same reading for both models as they were located near the inlet ports and the effect of inlet velocity boundary conditions was more dominant than the mixing process.

3 Mathematical modelling

Steady-state conditions, single-phase, laminar flows were considered for the liquid flowing through the microchannels. The governing differential Eqs.(4)-(7) describe the hydraulic and thermal behaviour by omitting the body force term.

Continuity equation:

$$\frac{\partial u}{\partial x}+\frac{\partial v}{\partial y}+\frac{\partial w}{\partial z}=0 \qquad (4)$$

Navier-Stokes equations:

$$\rho\left(u\frac{\partial u}{\partial x}+v\frac{\partial u}{\partial y}+w\frac{\partial u}{\partial z}\right)=-\frac{\partial p}{\partial x}+\mu\left(\frac{\partial^2 u}{\partial x^2}+\frac{\partial^2 u}{\partial y^2}+\frac{\partial^2 u}{\partial z^2}\right) \qquad (5)$$

$$\rho\left(u\frac{\partial v}{\partial x}+v\frac{\partial v}{\partial y}+w\frac{\partial v}{\partial z}\right)=-\frac{\partial p}{\partial y}+\mu\left(\frac{\partial^2 v}{\partial x^2}+\frac{\partial^2 v}{\partial y^2}+\frac{\partial^2 v}{\partial z^2}\right) \qquad (6)$$

$$\rho\left(u\frac{\partial w}{\partial x}+v\frac{\partial w}{\partial y}+w\frac{\partial w}{\partial z}\right)=-\frac{\partial p}{\partial z}+\mu\left(\frac{\partial^2 w}{\partial x^2}+\frac{\partial^2 w}{\partial y^2}+\frac{\partial^2 w}{\partial z^2}\right) \qquad (7)$$

The energy equation describes heat flow through the liquid and solid by considering convection terms in the equation as follows:

$$\rho\ Cp\ (u\frac{\partial T}{\partial x}+v\frac{\partial T}{\partial y}+w\frac{\partial T}{\partial x})=k\ (\frac{\partial^2 T}{\partial x^2}+\frac{\partial^2 T}{\partial y^2}+\frac{\partial^2 T}{\partial z^2}) \quad (8)$$

3.1 Boundary conditions

3.1.1 Hydraulic boundary conditions

Two inlet velocity boundary conditions were investigated, one with a uniform inlet velocity,

$$\boldsymbol{u} = -U_o\boldsymbol{n} \quad (9)$$

where the normal vector $\boldsymbol{n}$ is pointed to the outlet of the boundary, and other with a fully developed inlet velocity [35],

$$U_{uni}=2U_{avg}\left(1-\frac{r^2}{R^2}\right) \quad (10)$$

At the outlet boundary, gauge pressure was set equal to zero

$$p = p_o \quad (11)$$

thus representing an imposed pressure on the outlet boundary.

Non-slip boundary conditions were used for the solid-liquid interaction wall(s):

$$\boldsymbol{u} = 0 \quad (12)$$

3.1.2 Thermal boundary conditions

For the thermal boundary conditions, a constant inlet temperature was imposed at the inlet ports of the microchannels:

$$T = T_o \quad (13)$$

Heat supplied by the microheaters is represented by the following boundary conditions

$$\boldsymbol{n} \cdot (k\ \boldsymbol{\nabla} T) = q_o \quad (14)$$

where $q_o\ [W/m^2]$ represents the heat flux normal to the boundary which could be heat generated from the electric heater.

The solid liquid interaction boundary condition is written as follows

$$\boldsymbol{n} \cdot (k\ \boldsymbol{\nabla} T) = h(T_f - T_s) \quad (15)$$

where $h\ [W/m^2\ K]$ are $T_f[K]$ and $T_s[K]$ are the convection heat transfer coefficient, fluid and surface temperature, respectively.

Finally, convective boundary which is applied at the exit ports of the manifold was defined as

$$q_{cond} \cdot n = -k\, \nabla T \cdot n = 0, \qquad q_{conv} \cdot n = \rho\; Cp\;\; \nabla T\; u \cdot n \tag{16}$$

Note that Eq.(16) assumes an adiabatic condition for the solid exit boundaries and that all heat is totally extracted by convection.

4 Numerical analysis

The following assumptions were made in the numerical simulations used in analysis of the experimental cooling device(s):

1. The effect of heat transfer through the lid was ignored due to the lid's low thermal conductivity, allowing computational time to be saved.
2. The numerical model assumed that the channel cross-section was a right-angled rectangular shape, whereas, the actual geometry may have some deviation from this due to the CNC machining process.
3. Model(s) internal surfaces were assumed to be smooth.
4. The average heat loss was assumed to be equal for each single micro-heater.
5. The calculated surface temperature from the numerical simulations was an average temperature taken at multiple points on a surface square with side length that equalled the probe diameter.
6. It was assumed that the thermocouple probe measures temperature at its surface, rather that its junction which may be found inside the body of the thermocouple probe. Moreover, a perfect contact between the probe and the surface was assumed.

4.1 Boundary conditions and water properties

An average inlet velocity was adopted from the experimental results as listed in Table 2. Heat fluxes were applied to an area of size 12 mm × 15.5 mm, where the area of each hotspot was 4 mm × 15.5 mm. The effective area of each micro-heater, excluding the blue region (micro-heater wiring), was equal to 2mm×8mm (See Fig. 2). The average effective length of 8 mm was used for all microheaters. The average power provided to the middle sets of microheaters (H2 & H5) was 11.25W and 3W for each off-centre set H1& H4 and H3 & H6. Applied heat fluxes are shown in Table 3. DI water was chosen as the working liquid and its properties were temperature dependent.

4.2 Meshing procedures and mesh dependency test

Navier-Stokes and energy Eqs.(5)-(8) have been solved numerically by using COMSOL Multiphysics based finite elements numerical method (FEM). A free meshing process with tetrahedral mesh elements was chosen because of the irregular geometry of the model. The number of elements was increased at the entrance to the channels and on the interaction surface in order to capture the flow conditions at these locations. COMSOL uses Galerkin method to convert the above partial differential equations (PDEs) into an FEM integral form [36].

Fig. 7 shows the mesh element density used in the model with and without subchannels. Moreover, COMSOL Multiphysics provides a tool which is called mesh quality and used to ensure that the meshing quality does not affect the solution (See

Fig. 7) [37]. The system of the model equations were solved using an iterative linear solver GMRES (generalized minimum residual) with multigrid preconditioner.

Fig. 8A shows a negligible change in the pressure results for three sets of mesh elements, whereas the mesh independent solution was only obtained for both the velocity and

temperature distributions when the number of mesh elements was equal to 1,737,391. Therefore, 1,737,391 elements were used for subsequent numerical analysis. The same trend is shown in Fig. 8B for the model with subchannels where 2,243,226 elements were used to ensure a mesh independent solution.

4.3 Manifold bottom surface temperature results

A. Model without subchannels

Fig. 9a shows a good agreement between the numerical and experimental results for the three thermocouples (*Thermocouple 1*, *Thermocouple 2*, and *Thermocouple 3*) and for both the inlet boundary conditions (uniform and fully developed velocity). However, a small deviation can be seen for *Thermocouple 3* with the uniform boundary conditions. We propose that *Thermocouple 3* gave a lower temperature reading as its contact area in the numerical simulation was considered to be larger than the actual contact area or, its active junction was not in full contact with surface.

Fig. 9b shows good agreement between the experimental and numerical results for the thermocouples (*Thermocouple 4*, *Thermocouple 5* and *Thermocouple 6*). *Thermocouple 5* shows a small deviation from experimental data for the boundary conditions of fully developed inlet velocity. *Thermocouple 5* is located at the mid-line between the inlet ports where the two inlet streams are mixed. In this situation, assuming fully developed flow as a boundary condition for the numerical method may under-predict the temperature due to the mixing condition at this point. Consequently, numerical results could give a lower temperature for this thermocouple. Fig. 9(a-b) also shows that there is no major difference in the numerical results between the uniform and fully developed inlet velocity boundary conditions. The flow entered through the inlet ports and deviated by 90° before being redistributed through the inlet manifold. Consequently, the inlet velocity boundary condition was invalidated when the flow left the inlet ports and entered the channels. The uniform inlet velocity was closer to the true case than the fully developed boundary as the plastic tube was not straight before connecting to the inlet ports.

B. Model with subchannels

A good agreement was obtained for the simulations of *Thermocouple 1*, *Thermocouple 2* and *Thermocouple 3* when compared to the experimental results for both the inlet velocity conditions as shown in Fig. 10a. Another validation of the numerical results was achieved for *Thermocouple 4*, *Thermocouple 5* and *Thermocouple 6* when compared to the experimental data (See Fig. 10b) with only a small deviation for *Thermocouple 4*.

C. Percentage deviation of the numerical results

Fig. 11a shows the percentage deviations between the experimental data and the numerical results for the model without subchannels using the uniform inlet velocity boundary condition. It also shows that each thermocouple had a different percentage error for each pressure head since each thermocouple measured temperature at different locations (See Fig. 2). Furthermore, the actual contact area between probe and the surface was different for each thermocouple which altered their thermal contact resistance [28]. Accordingly, it is possible to see a different percentage error for each thermocouple.

The same trend in percentage deviation for the subchannels model is shown in Fig. 11b. This is considered to be the result of the same sources of errors as described for the previous model. However, the result for Thermocouple 4 from the model with subchannels under-

predicts the temperature reading (See Fig. 10b) and gives a higher percentage error. In particular, *thermocouple 4* shows a maximum deviation of 5% in comparison with the other thermocouples. This may be due to variations in the individual contacts between the microheaters and the bottom surface of copper channels leading to a higher reading for any thermocouple near that point.

4.4 Analysis of numerical results

Fig. 12 shows numerical results for the bottom surface temperature of the channels along the full model. It shows that the maximum temperature occurs downstream of the hotspot. Thermal and hydraulic boundary layers were re-created at the entrance to subchannels due to the presence of an obstacle (in this instance, the subchannels) in the flow direction.

The thickness of the thermal boundary layer increased towards the end of the subchannels. Consequently, heat transfer rate was increased upstream and gradually decreased downstream through the subchannels (See section 4.4.1). The same behaviour was applicable to the model without subchannels except the maximum temperature occurred earlier. A comparison between Fig. 12 and Fig. 13 reveals that the maximum temperature occurred approximately at the axial position of 7.5cm for the model without subchannels and at 8cm for the model with subchannels. Adding subchannels led to a reduction in the maximum surface temperature from 32.5^{o}C to 29°C. Furthermore, temperature uniformity was improved by reducing the difference between the maximum and minimum temperatures from ~5°C (without subchannels) to ~2.5^{o}C (with subchannels). Fig. 14a shows the velocity and temperature distribution at a plane across the middle height of the channels for the model without subchannels. It also shows that only a thin layer of liquid was affected by the heat transfer from the channel walls while the temperature of the rest of the liquid had an approximately constant temperature. The fluid boundary layer developed at the channel inlet leading to a sharp increase in velocity and a nearly fully developed flow downstream of the channel as shown in Fig. 8A.

However, a different behaviour can be seen for the system with subchannels as shown in Fig. 14b. The flow before the subchannels exhibited similar behaviour to the model without subchannels, but exhibited a rapid increase in flow velocity through the subchannels due to their area reduction (See Fig. 14). The presence of the subchannels both accelerated flow and increased the heat transfer area. Moreover, the model with subchannels shows better thermal performance with a lower temperature.

4.4.1 Nusselt number`

Nusselt number (Nu) provides a deep understanding of the effect of subchannels on the system thermal performance. Nu is calculated from Eq.(17) [38]

$$Nu=\frac{D_h}{k_f}\frac{q^{"}}{T_{w,avg}-T_{b,avg}} \tag{17}$$

where $T_{b,avg}$ is calculated from Eq.(18) and $T_{w,avg}$ is calculated from Eq.(19)

$$T_{b,avg} = \frac{\int \rho TudA}{\int \rho udA} \quad (18)$$

$$T_{w,avg} = \frac{1}{L} \int_L T_w \, dl \quad (19)$$

The middle channel was specifically chosen to calculate *Nu* for comparison, allowing us to save computational time. Fig. 15a shows the variation of *Nu* along the channel axis for the model without subchannels. The developed thermal boundary layer is thin at the channel inlet indicating a high transfer rate was taking place. Subsequently, there was a sharp increase in *Nu* at the channel entrance as shown in Fig. 15a. Thereafter, a gradual drop in *Nu* was predicted due to the effect of the developing thermal boundary layer. In addition, the hotspot which caused a small variation in the value of *Nu* at the middle of the channels is also shown.

A different behaviour of *Nu* was predicted for the model with subchannels as shown in Fig. 15b. Three distinct behaviours of *Nu* are seen in the upstream, middle and downstream of the channels. The entrance effect is also obvious on the *Nu* value(s) and then the gradual drop as a result of the effect of developing boundary layers, as already described. Subchannels above the hotspot enhance the heat transfer rate due to the increase in solid-liquid interaction. Moreover, the thermal boundary layer(s) were disrupted when the flow reached the subchannels. Therefore, new thermal and hydraulic boundary layers started to form at the entrance to the subchannels. This caused a sharp jump in the *Nu* value(s) at the subchannels' inlet (See Fig. 15b). The small jump in *Nu* at the exit of the subchannels was a result of flow circulation, following this there was then a sharp drop in *Nu* at inlet to downstream subchannels (See Fig. 15b). A comparison between Fig. 15a and Fig. 15b shows that the model with subchannels indicates improved performance.

4.4.2 Pumping power and thermal resistance

Pumping power and thermal resistance were calculated from Eqs.(20) and (21) respectively [39].

$$Po = \Delta p * \frac{\dot{m}_w}{\rho} \quad (20)$$

$$R_{th} = \frac{\Delta T_{max}}{q''_{uniform} \times A_{uniform} + q''_{spot} \times A_{spot}} \quad (21)$$

The pumping power calculation depends on numerical data to measure the pressure difference across the model. Pumping power rises are a result of the increase in the pressure drop in the presence of subchannels. The inserting of the subchannels in the middle of the main channels creates an obstacle to the fluid flow and a circulation will be generated at entrance to the subchannels. Moreover, the reduction in channel(s) cross-sectional area to one-third of the main channel area led to an increase in the pressure drop thus a higher pumping power will be required. The effect of the subchannels will be more complex with the increase in the mass flow rate and therefore higher pressure drop was generated and pumping power was required as shown in Fig. 16a.

Fig. 16b shows a comparison between thermal resistance and pressure drop for both models for the same range of pressure head, see section 2.4. The thermal resistance decreases following the drop in the maximum surface temperature for the model with subchannels. Fig. 16b demonstrates that for the same pressure head (see section 2.4) the model with

subchannels produces more pressure drop but with lower thermal resistance (Eqs.(22) and (23) are the best fit equations which describe the variation of thermal resistance with pressure drop. Eqs.(22) and (23) can predict the amount of improvement in thermal resistance for a specific pressure drop (for both models) without having to carry out additional experimental or simulation analyses. For a specific model a compromise between the effect of adding subchannels on thermal resistance and pressure drop which can decide the benefit of using subchannels. Its shown in Fig. 16b that for the same pressure head 79cm the thermal resistance has been reduced 20% whereas the pumping power increased by 11%.

For the model without subchannels the thermal resistance can be written as

$$R_{th,\ No}=3.2\ \Delta p^{-0.29} \tag{22}$$

and for the model with subchannels

$$R_{th,\ with}=3.76\ \Delta p^{-0.35} \tag{23}$$

4.5 Conclusions

The continuously increasing technological improvements in integrated circuit performance is typically associated with increased heat generation, requiring more effective methods for its removal. In addition, the heat fluxes generated above a chip are often non-uniform, requiring enhanced heat extraction above particular high heat flux regions.

This work shows that the inclusion of subchannels into a liquid cooled heat sink reduces the maximum surface temperature and improves temperature uniformity. Model(s) of two inlet and outlet ports were fabricated in order to obtain an approximately uniform mass flow rate distribution through channels. This allowed the following conclusions to be reached:

- The surface temperature distribution was improved for the model with subchannels in comparison to that without subchannels. Consequently, the difference in the temperature along the surface was reduced. Moreover, the model with subchannels showed lower maximum surface temperature.
- The maximum surface temperature occurred upstream of the subchannel section because of the flow direction.
- The model with subchannels had a lower thermal resistance in comparison to the model without.
- The required pumping power increased as a result of the addition of the subchannels.
- The experimental and numerical results can be adopted to predict the amount of improvement in thermal resistance for a specific pressure drop (for both models) without the need for additional experimental or simulation analyses, see Eqs.(22) and (23). Eqs.(22) and (23) are applicable when the size of the subchannels (or hotspot) is one third of the size of the main channels.

The advantage of the approach presented is that it offers the same, commonly employed parallel channel configuration with a simple design change to add subchannels above the hotspot. This simplicity means that the subchannels can be added wherever the hotspot is present with no need to change the design in other regions.

Acknowledgement
The authors would like to thank The Ministry of Higher Education and Scientific Research / IRAQ for their financial support.

References

[1] D. B. Tuckerman and R.F.W Pease, IEEE Electron Device Letters, "High-Performance Heat Sinking for VLSI", May 1981, vol. EDL-2, no. 5, DOI: 10.1109/EDL.1981.25367.

[2] M. C. Lu and C. C. Wang, IEEE Transactions on Components and Packaging Technologies, "Effect of the Inlet Location on the Performance of Parallel-Channel Cold-Plate", March 2006, vol. 29, no. 1, pp. 30-38, DOI: 10.1109/TCAPT.2005.850539.

[3] Z. Azizia, A. Alamdari and M.R. Malayeri, Applied Thermal Engineering, "Thermal performance and friction factor of a cylindrical microchannel heat sink cooled by Cu-water nanofluid", 2016, vol. 99, pp. 970–978, DOI: http://dx.doi.org/10.1016/j.applthermaleng.2016.01.140.

[4] Z. Azizi, A. Alamdari and M.R. Malayeri, Energy Conversion and Management, "Convective heat transfer of Cu–water nanofluid in a cylindrical microchannel heat sink ", 2015, vol. 101, pp. 515–524, DOI: http://dx.doi.org/10.1016/j.enconman.2015.05.073.

[5] P. G. Hegde and K.N. Seetharamu, Electronic Manufacturing Technology Symposium (IEMT), 2008 33rd IEEE/CPMT International, "Effects of Non-Uniform Base Heating in Multi Stack Microchannel Heat Sinks Used for Cooling High Heat Flux Electronic Chips and Devices", 4-6 November 2008, Penang, DOI: 10.1109/IEMT.2008.5507856.

[6] X. Wei, "Stacked Microchannel Heat Sinks for Liquid Cooling Microelectronics Devices", PhD thesis, November 2004, Mechanical Engineering, Georgia Institute of Technology, DOI: hdl.handle.net/1853/4873.

[7] A. Chauhan, B. Sammakia, K. Ghose, G. R. Ahmed and D. Agonafer, 12th IEEE Intersociety Conference, Thermal and Thermomechanical Phenomena in Electronic Systems (ITherm), "Hot Spot Mitigation Using Single-Phase Microchannel Cooling For Microprocessors", 2-5 June 2010, Las Vegas, NV, DOI: 10.1109/ITHERM.2010.5501357.

[8] G. Xie, S. Li, B. Sunden and W. Zhang, International Journal for Numerical Methods in Heat & Fluid Flow, "Computational Fluid Dynamics for Thermal

Perfomance of a Water-Cooled minichannel Heat Sink with Different Chip Arrangements", 2014, vol. 24, no. 4, pp. 797 - 810, DOI: dx.doi.org/10.1108/HFF-01-2013-0013.

[9] L. Biswal, S. Chakraborty and S.K. Som, IEEE Transactions on Components and Packaging Technologies, "Design and Optimization of Single-Phase Liquid Cooled Microchannel Heat Sink", 04 December 2009, vol. 32, no. 4, pp. 876-886, DOI: 10.1109/TCAPT.2009.2025598.

[10] R. Prasher and J. Y. Chang, Proceedings of the Sixth International ASME Conference on Nanochannels, Microchannels and Minichannels, ICNMM2008, "Cooling of Electronic Chips Using Microchannel and Micro-Pin Heat Exchangers", June 23-25 2008, Darmstadt, Germany, DOI: 10.1115/ICNMM2008-62384.

[11] Z. Minliang, W. Xiaojing, L. Hongjun and W. Guoliang, International Conference on Electronic Packaging Technology and High Density Packaging ICEPT-HDP 2008, "Numerical Simulation of the Micro-Channel Heat Sink on Non-Uniform Heat Source", 28-31 July 2008, Shanghai IEEE, DOI: 10.1109/ICEPT.2008.4606946.

[12] X. Wang, W. Zhang, H. Liu, L. Chen and Z. Li, International Conference on Electronic Packaging Technology and High Density Packagning ICEPT-HDP09, "Numerical Simulation on Variable Width Multi-Channels Heat Sinks with Non-Uniform Heat Source", 10-13 August 2009, Beijing IEEE, DOI: 10.1109/ICEPT.2009.5270609.

[13] Y. Zhang, Y. Li, X Li and S. Yao, Proceedings of the ASME 2013 Heat Transfer Summer Conference HT2013, "Strip-And-Zone Micro-Channel Liquid Cooling of Integrated Circuits Chips with Non-Uniform Power Distribution", July 14-19 2013, Minneapolis, MN, USA, DOI: 10.1115/HT2013-17311.

[14] Y. Li, D. Guo and S. C. Yao, Journal of Electronic Packaging, "Thermal-Aware Microchannel Cooling of Multicore Processors: A Three-Stage Design Approach", June 2014, vol. 136, DOI: 10.1115/1.4027174.

[15] G. Türkakar and T. O. Özyurt, International Journal of Thermal Sciences, "Dimensional Optimization of Microchannel Heat Sinks with Multiple Heat Sources", December 2012, vol. 62, pp. 85-92, DOI: 10.1016/j.ijthermalsci.2011.12.015.

[16] C. S. Sharma, G. Schlottig, T. Brunschwiler, M. K. Tiwari, B. Michel, and D. Poulikakos, International Journal of Heat and Mass Transfer, "A Novel Method of Energy Efficient Hotspot-Targeted Embedded Liquid Cooling for Electronics: An

experimental Study", 2015, vol. 88, pp. 684–694, DOI: 10.1016/j.ijheatmasstransfer.2015.04.047.

[17] R. Dias and L. Skoglund, Publication, P.A., "Variable Depth Microchannels", 27 March 2008.

[18] K. Goodson, T. Kenny, P. Zhou, Upadhya, M. Munch, M. McMaster, and J. Horn, United States Patent, No. US 7,104,312, B2, "Method and Apparatus for Achieving Temperature Uniformity and Hot Spot Cooling in a Heat Producing Device", September 12 2006, vol.

[19] Y. J. Lee, P. S. Lee and S. k. Chou, International Mechanical Engineering Congress & Exposition IMECE2010, "Hot Spot Mitigating Oblique Finned Microchannel Heat Sink", November 12-18 2010, Vancouver, British Columbia, Canada IEEE, DOI: 10.1109/TCPMT.2013.2244164.

[20] Y. J. Lee, P. S. Lee and S. K. Chou, IEEE Transaction on Components, Packaging and Manfacturing Technology, "Hotspot Mitigating with Obliquely Finned Microchannel Heat Sink-An Experimental Study", 22 February 2013, vol. 3, no. 8, pp. 1332-1341, DOI: 10.1109/TCPMT.2013.2244164.

[21] Sabic Innovative Plastics, "Lexan sheet of number 9030", 05th April 2015, <https://sfs.sabic.eu/wp-content/uploads/resource_pdf/1345453948-48623687-Technical-Manual-Coated-Uncoated-Sheet.pdf>.

[22] Henkel Corporation, " Adhesive Epoxy LOCTITE® SI 5145™", 17th April 2015, <http://www.henkelna.com/about-henkel/product-search-1554.htm?nodeid=8797879926785>.

[23] Performance Plastics Corporation Saint-Goban, "Comprehensive Guide to Tygon® tubing Formulations", 2006,

[24] HERAEUS, "Pt 6,8 M1020, order number 32208172", 06-04-2015 2015, <http://heraeus-sensor-technology.com/en/produkte_1/sensormodule/sensor_module.aspx>.

[25] Mega Electronics Limited, "Fotoboard-Pre-Sensitised Copper Board", 18th April 2015, <http://www.megauk.com/>.

[26] Electrolube/ The solution People, "HTC, non-silicone thermal paste heat transfer compound, REF:HTC02S ", 6th April 2015, <www.electrolube.com >.

[27] CORNING, "Machinable Glass Ceramic-Macor", 16th of April 2015, <http://www.corning.com/specialtymaterials/advanced_optics/specialty_glass_ceramics/products/macor/index.aspx>.

[28] A. A. Y. Al Waaly, M. C. Paul and P. S. Dobson, Applied Thermal Engineering, "Effects of Thermocouple Electrical Insulation on the Measurement of Surface Temperature", 2015, vol. 89, pp. 421-431, DOI: 10.1016/j.applthermaleng.2015.06.020.

[29] R. A. Hart and A.K. da Silva, International Journal of Heat and Mass Transfer "Experimental Thermal–Hydraulic Evaluation of Constructal Microfluidic Structures under Fully Constrained Conditions", July 2011, vol. 54, no. 15-16, pp. 3661–3671, DOI: 10.1016/j.ijheatmasstransfer.2011.02.063.

[30] digitron of a brand of electron technology, "http://www.digitron.com/", 13th of April 2015,

[31] GW Instek, "Linear DC power supplies, GPS-x303 Series", 17th April 2015, <http://www.gwinstek.com.tw/en/product/productdetail.aspx?pid=38&mid=53&id=131>.

[32] American Society for Testing Materials, "Manual on the Use of Thermocouples in Temperature Measurement", 1993, 4th ed.

[33] Chander Shekhar Sharma, Manish K. Tiwari, Severin Zimmermann, Thomas Brunschwiler, Gerd Schlottig, Bruno Michel, and Dimos Poulikakos, Applied Energy, "Energy efficient hotspot-targeted embedded liquid cooling of electronics", 2015, vol. 138, pp. 414-422, DOI: http://dx.doi.org/10.1016/j.apenergy.2014.10.068.

[34] D. R. Lide, "CRC Handbook of Chemistry and Physics", Internet Version 2005, CRC Press, Boca, Raton, FL, 2005: http://www.hbcpnetbase.com,

[35] Aderian Bejan, "Convection Heat Transfer", 1995, 2nd ed., John Wiley & Sons, Incorporated.

[36] COMSOL AB., "COMSOL Multiphysics Reference Guide / v3.5a", 1998-2008.

[37] COMSOL AB, "COMSOL Multiphysics Modeling Guide / v3.5a", 1998-2008.

[38] W. Qu and I. Mudawar, International Journal of Heat and Mass Transfer, "Analysis of Three-Dimensional Heat Transfer in Micro-Channel Heat Sinks", September 2002, vol. 42, no. 19, pp. 3973-3985, DOI: 10.1016/S0017-9310(02)00101-1.

[39] D. Liu and S. V. Garimella, International Journal for Numerical Methods in Heat & Fluid Flow, "Analysis and Optimization of the Thermal Performance of Microchannel Heat Sinks", 2005, vol. 15, no. 1, pp. 7-26, DOI: 10.1108/09615530510571921.

[40] F. P. Incropera, D. P. Dewitt, T. L. Bergman and A. S. Lavine, "Fundamentals of Heat and Mass Transfer", 2007, Sixth, Jhon Wiley & Sons, Inc.

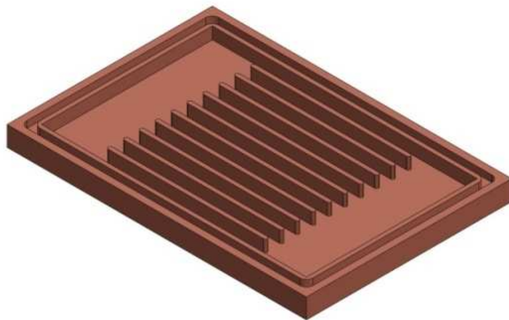

(a) without subchannels

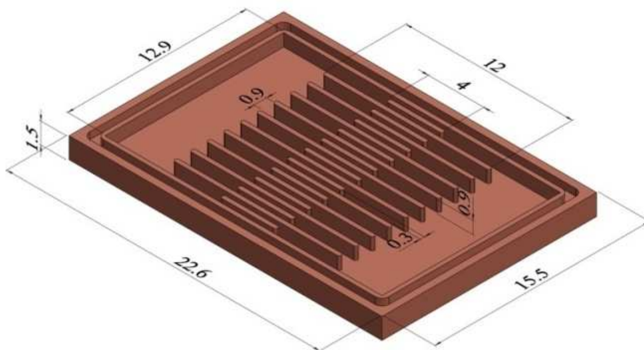

(b) with subchannels

Fig. 1 Models of microchannels: (a) without and with subchannels, all dimensions are in mm.

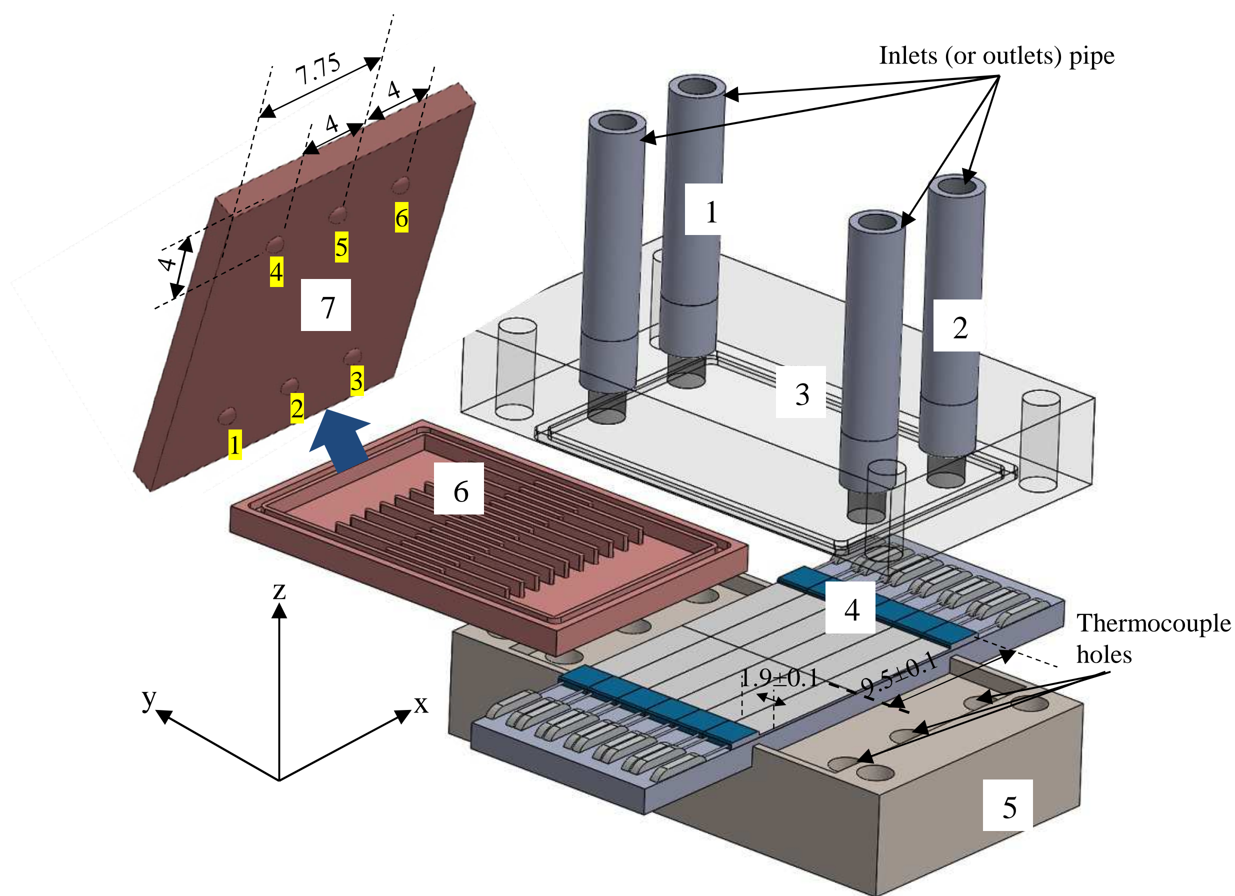

Fig. 2 Full geometry of the channels with subchannels: 1) and 2) inlet (or outlet ports), 3) lid, 4) microheaters and PCB, 5) base made of ceramic, 6) copper channels, and 7) positions of the thermocouples on the back of the channels. All dimensions are in mm.

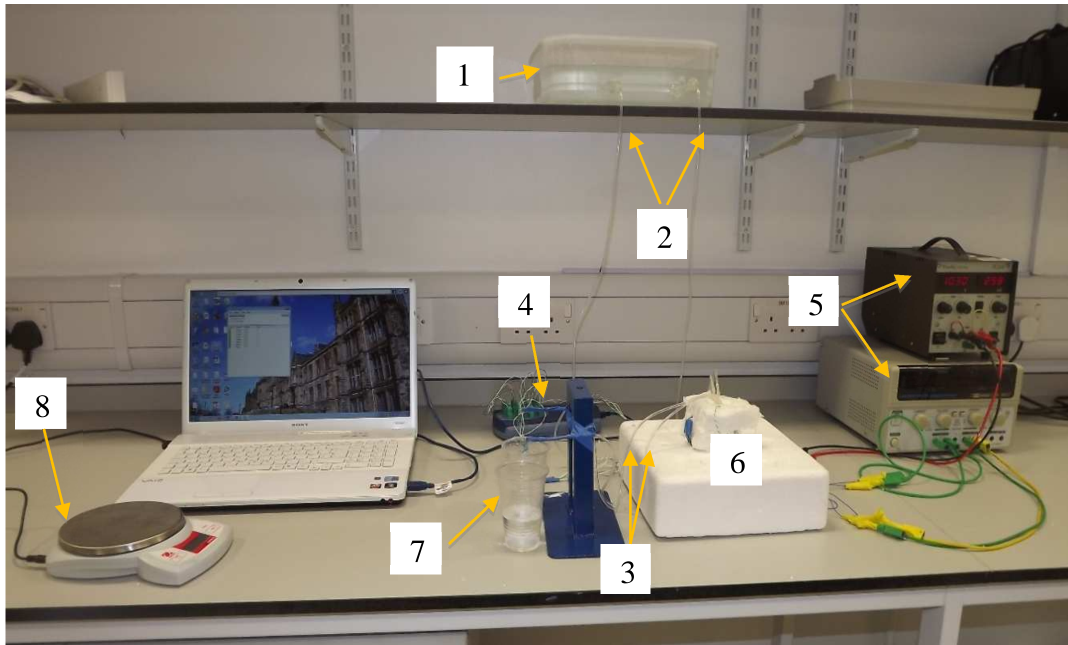

Fig. 3 Experimental setup: 1) water container, 2) plastic tubes feed water to the cooling device, 3) plastic tubes collect water from the cooling device, 4) pico TC-08 data logger, 5) power supplies, 6) cooling device with insulation, 7) water collection, 8) digital scale.

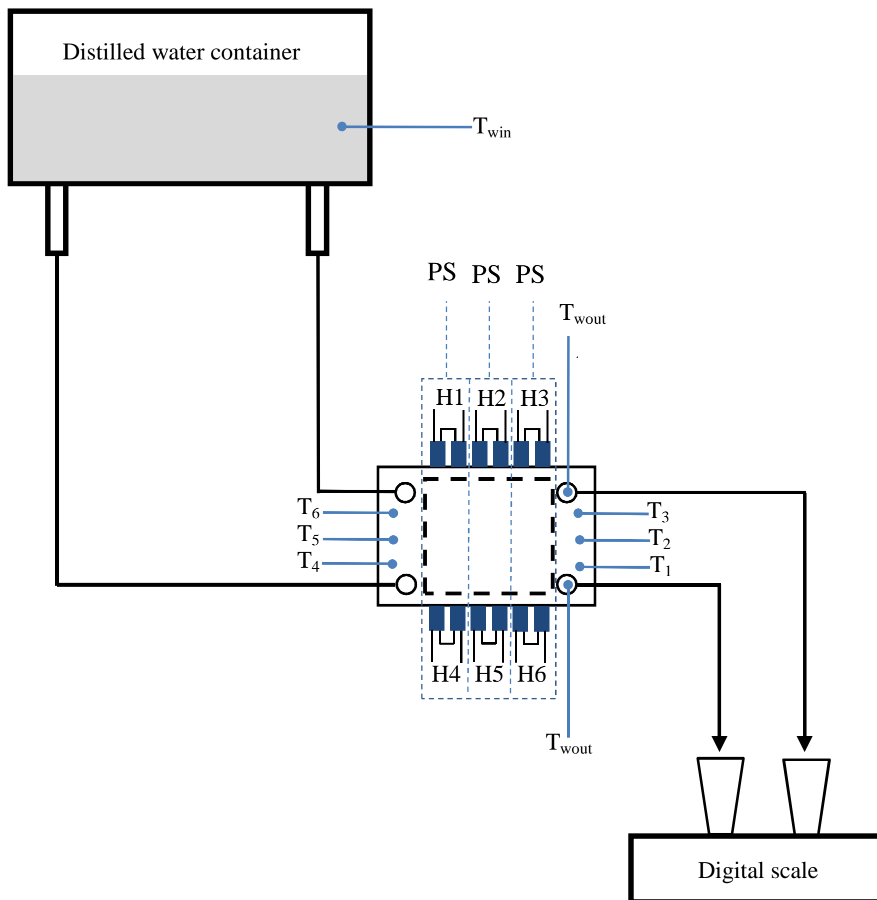

Fig. 4; Schematic diagram of the experimental setup H1to H6 representing pairs of heaters connected in series. Sets H1 & H4, H2 & H5 and H3 & H6 are connected in series.

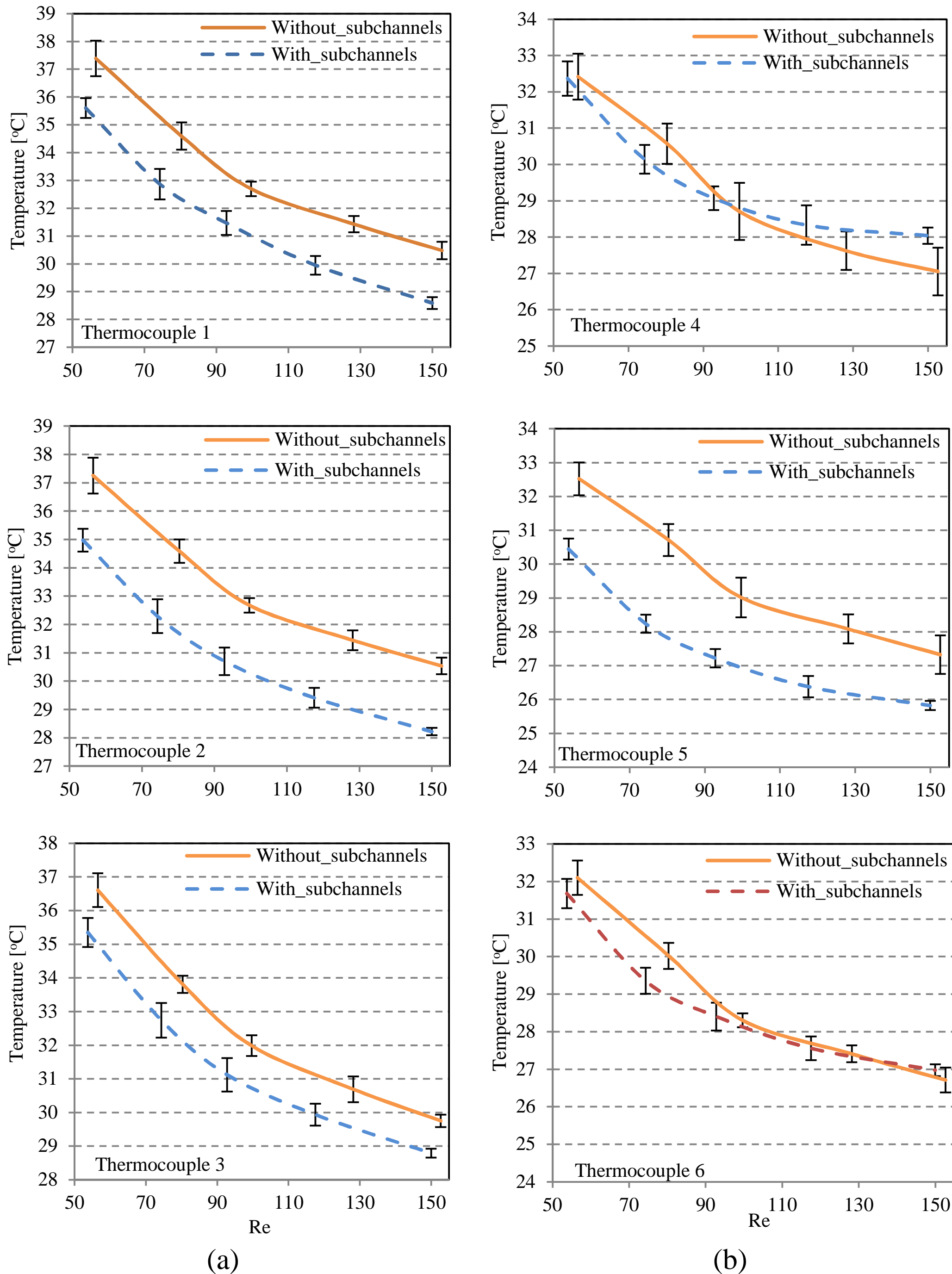

Fig. 5 Comparison of the experimental results with and without subchannels: (a) Thermocouple 1, Thermocouple 2 and Thermocouple 3 were attached to the bottom surface of the outlet manifold; while (b) Thermocouple 4, Thermocouple 5 and Thermocouple 6 were attached to the bottom surface of the inlet manifold. Error bars represent ± one standard deviation.

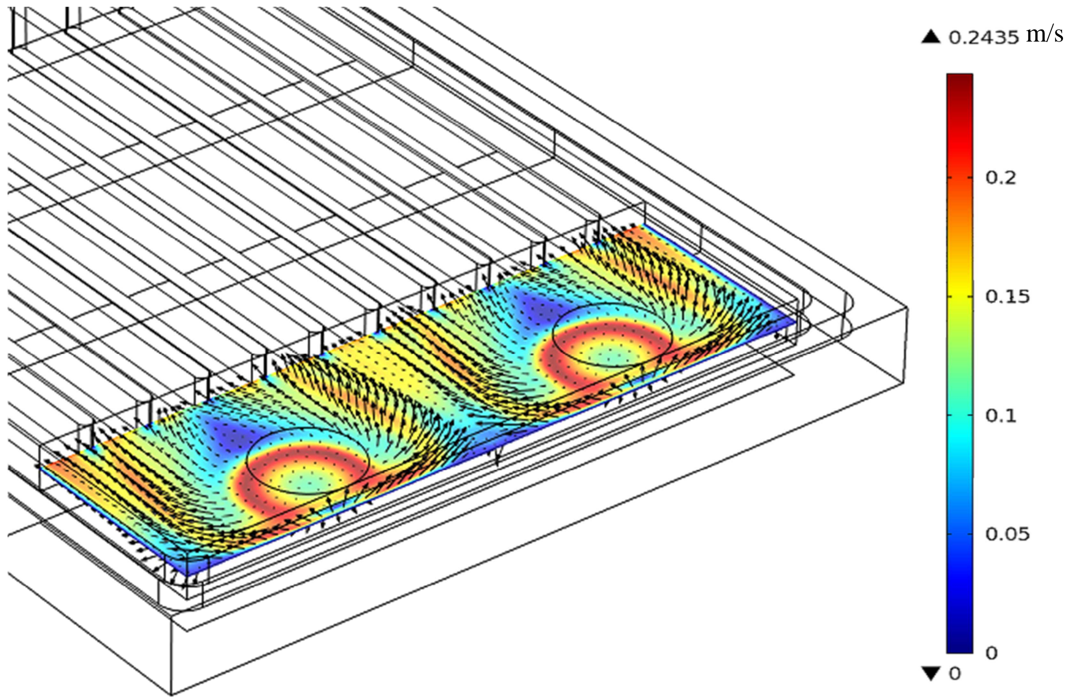

(a) **without** subchannels

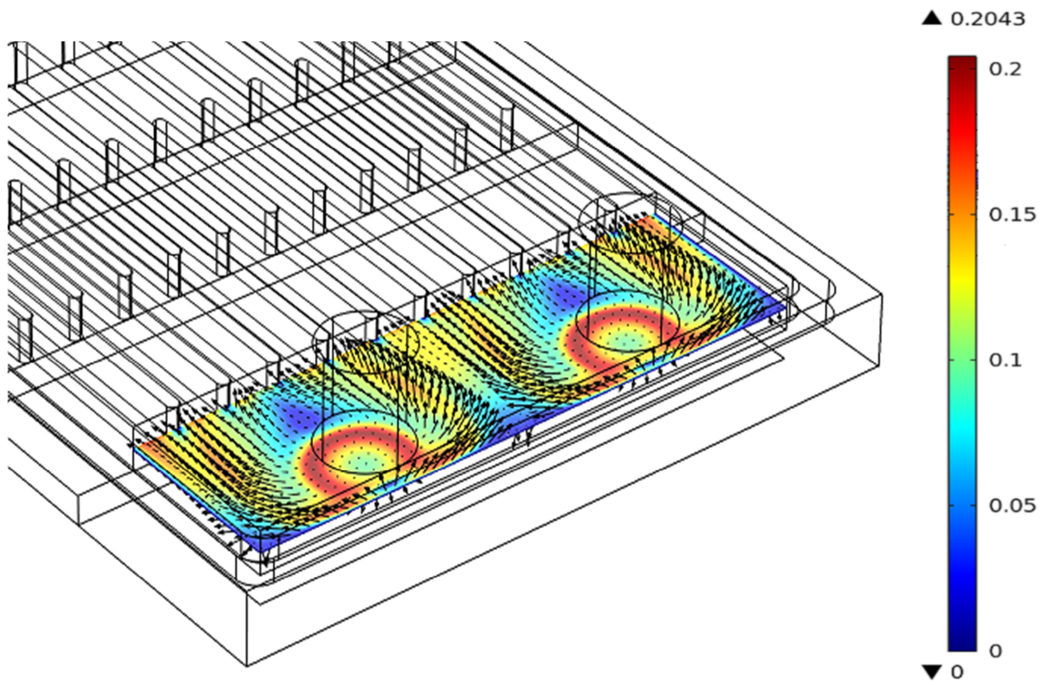

Fig.6 Velocity distribution and direction at inlet manifold for the model (a) **withoutt with** subchannels for the pressure head 75cm.

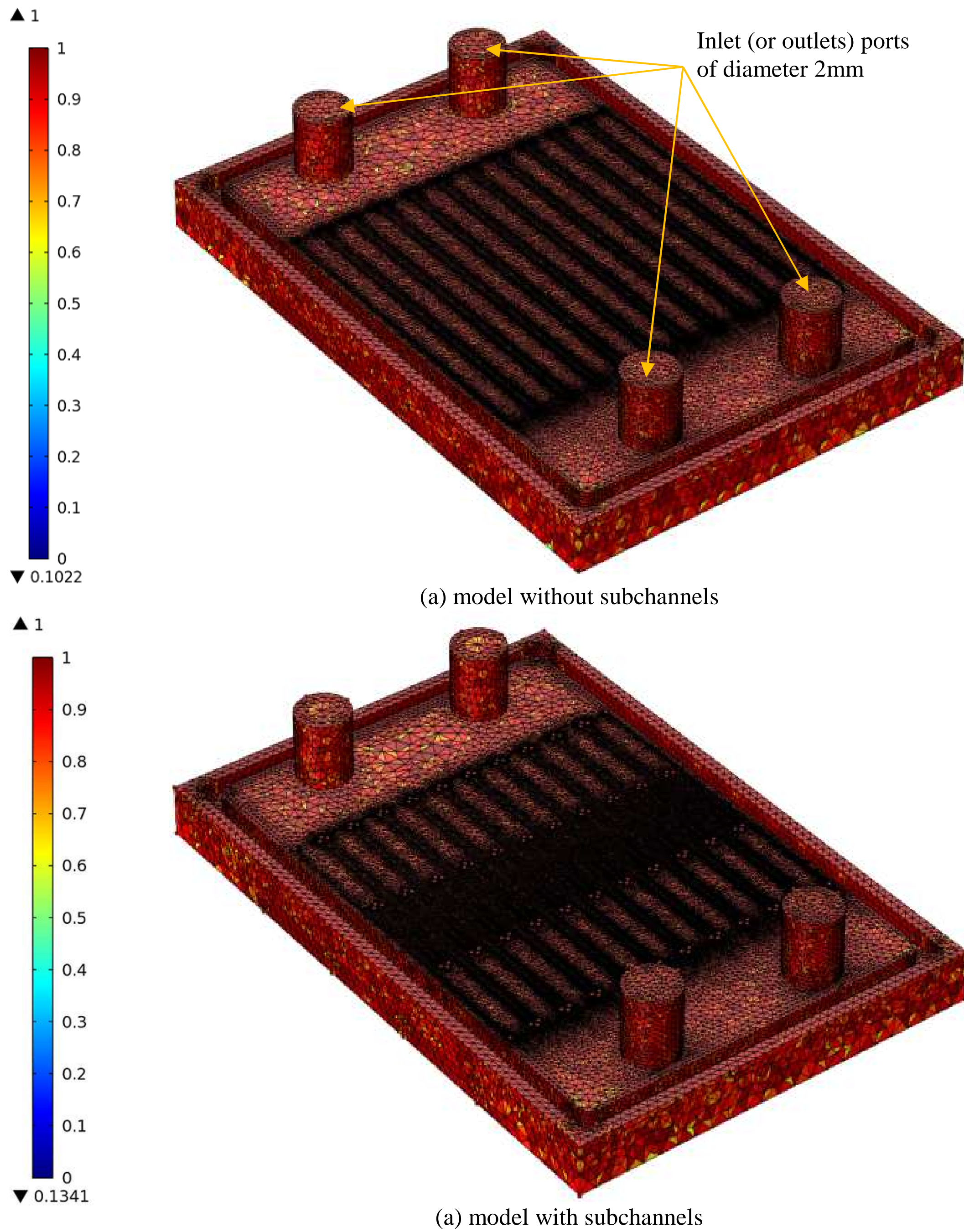

Fig. 7 Mesh elements quality for numerical analysis for both models **without** (a) and **with** (b) subchannels.

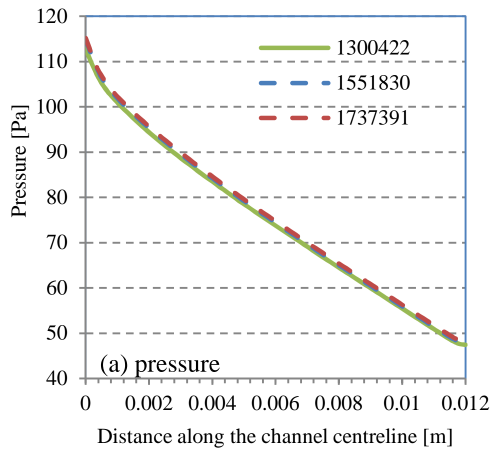

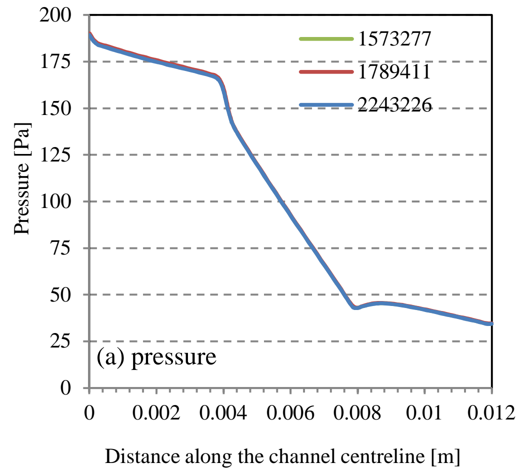

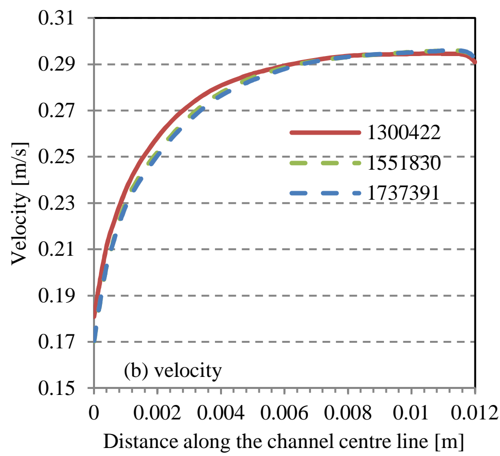

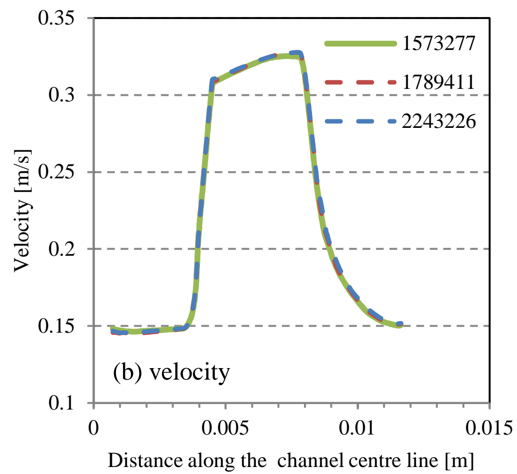

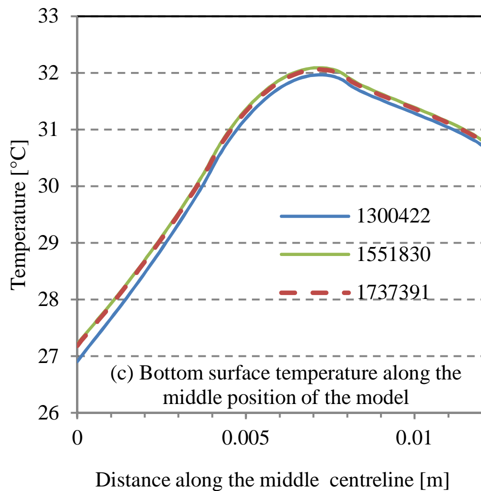

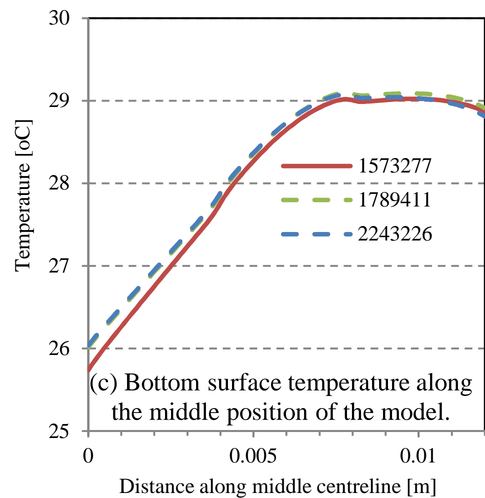

(A) Model without subchannels (B) Model with subchannels

Fig. 8 Numerical solutions at different mesh resolutions of the model: (A) without subchannels for *Re* = 152 and (B) with subchannels for *Re* = 149. (a) pressure, (b) velocity along the centreline of the middle channel and (c) Bottom surface temperature along the middle position of the model.

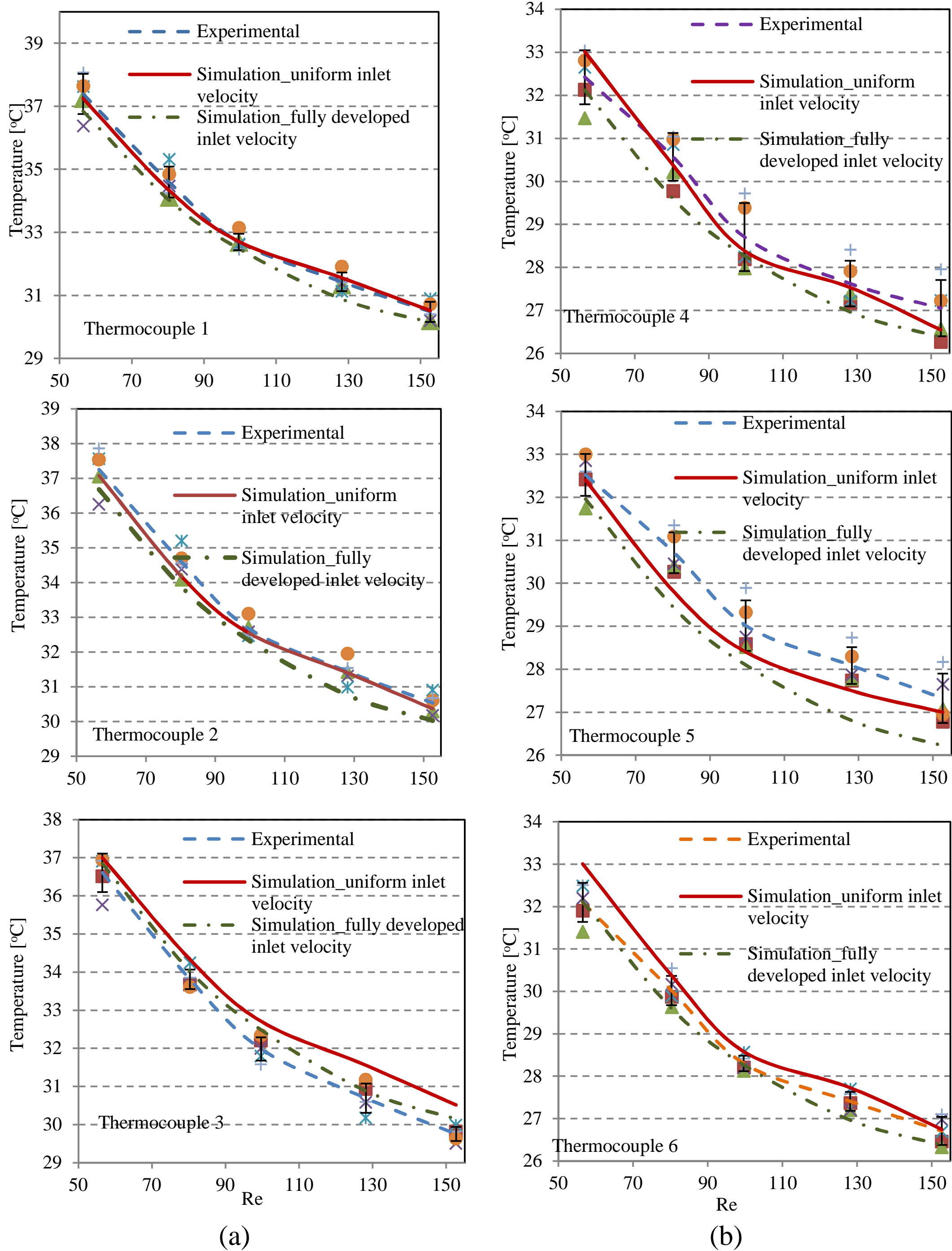

Fig. 9 Comparison between the experimental and simulation results of the models **without** subchannels of Thermocouple 1, Thermocouple 2, and Thermocouple 3 attached to the outlet manifold and of Thermocouple 4, Thermocouple 5, and Thermocouple 6 attached to the inlet manifold. Error bars represent ± one standard deviation.

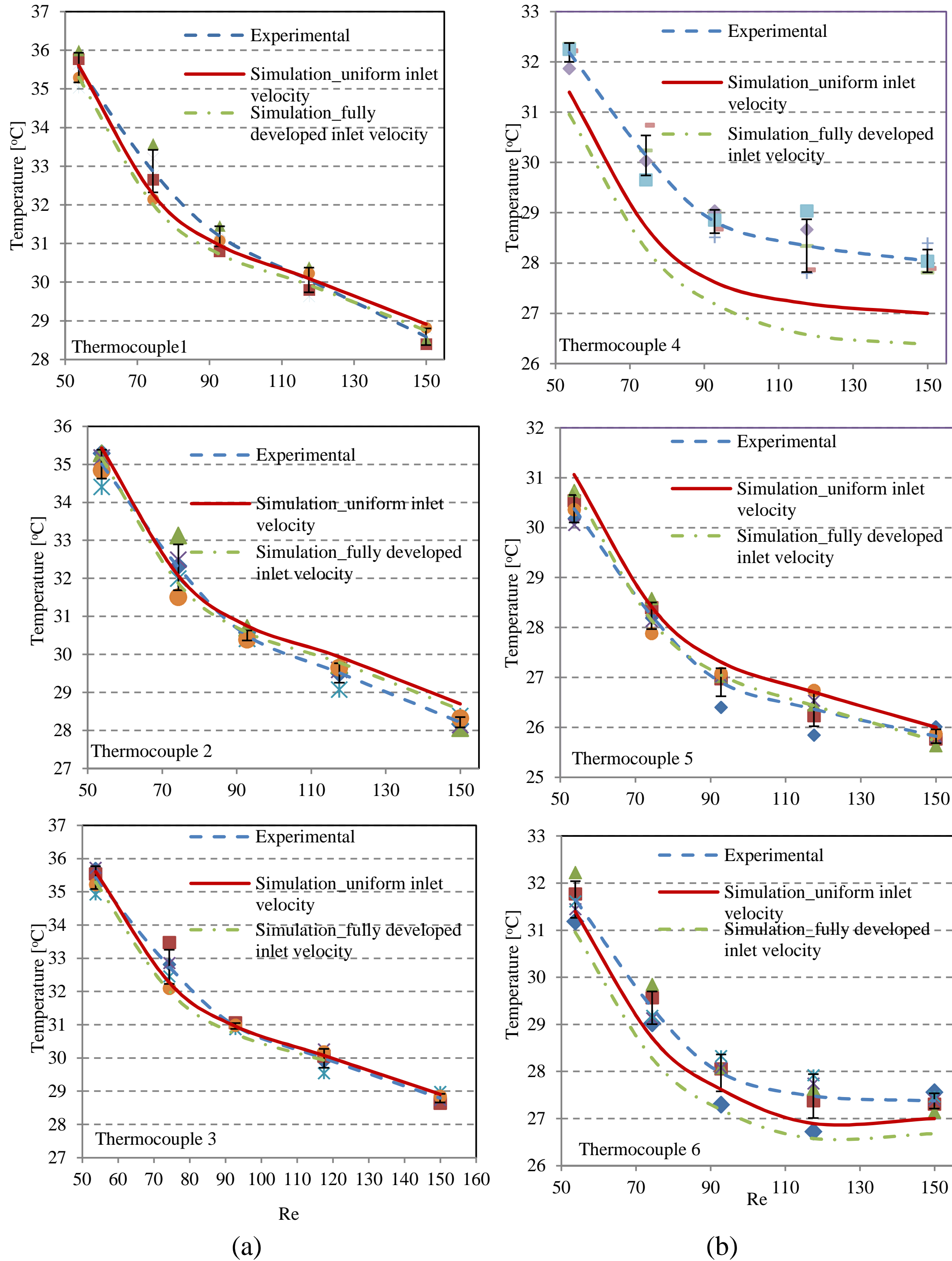

Fig. 10 Comparison between the experimental and simulation results of the models **with** subchannels of Thermocouple 1, Thermocouple 2, and Thermocouple3 attached to the outlet manifold and of Thermocouple 4, Thermocouple 5, and Thermocouple 6 attached to the inlet manifold. Error bars represent ± one standard deviation.

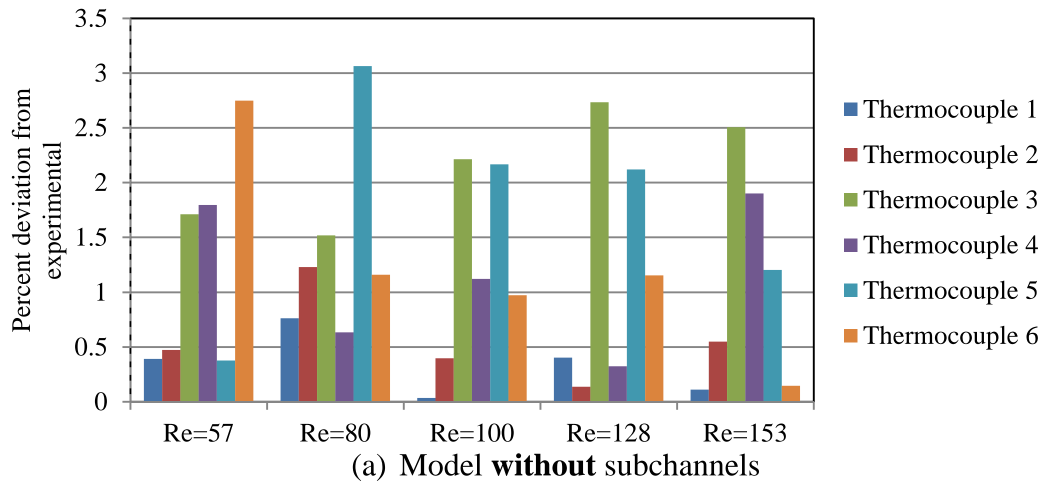

(a) Model **without** subchannels

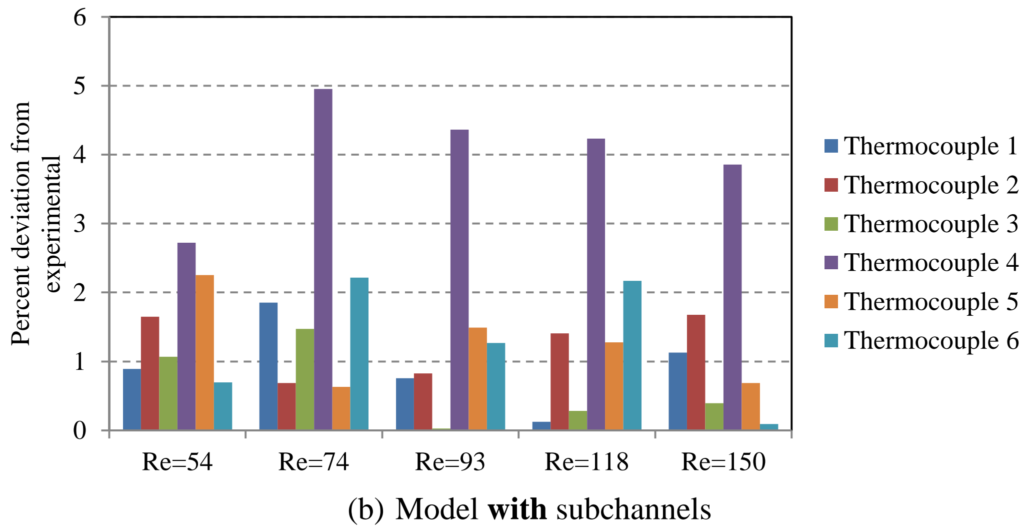

(b) Model **with** subchannels

Fig. 11: Percentage deviation of thermocouple readings from the experimental data for different pressure heads for the models: (a) without and (b) with subchannels.

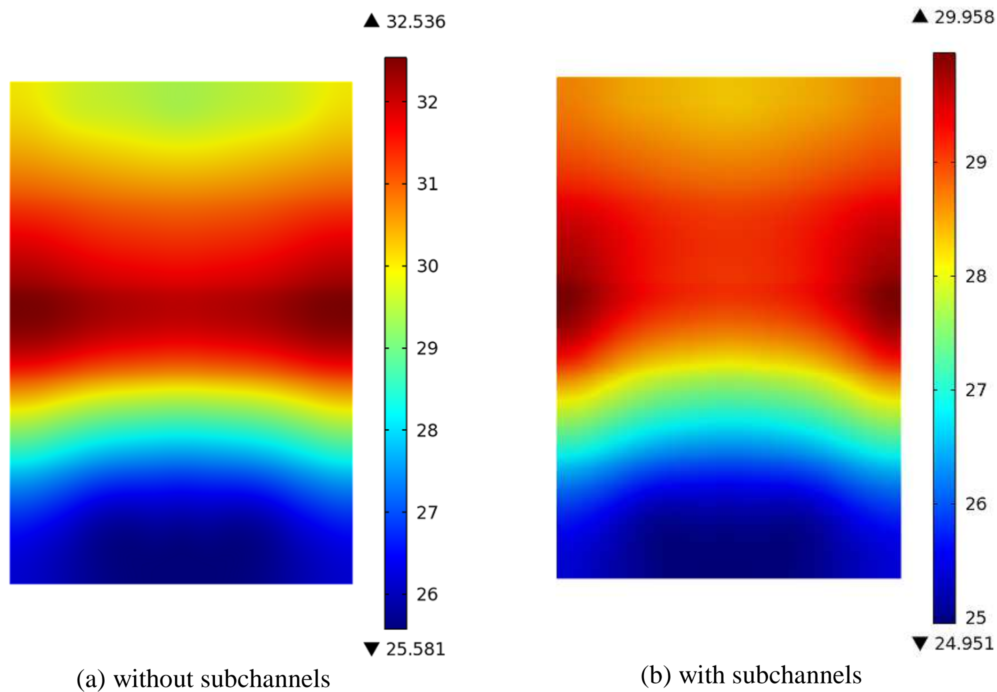

(a) without subchannels (b) with subchannels

Fig. 12 Temperature of the bottom surface under the copper plate for both models at the highest pressure head (79cm).

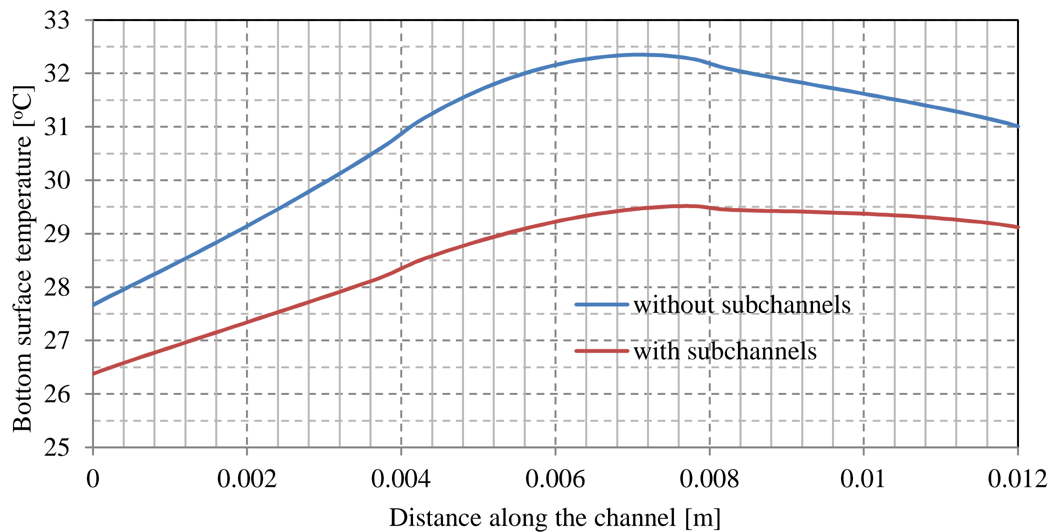

Fig. 13 Variation of the average bottom surface temperature along the channels for both the models with and without subchannels at the highest pressure head (79cm).

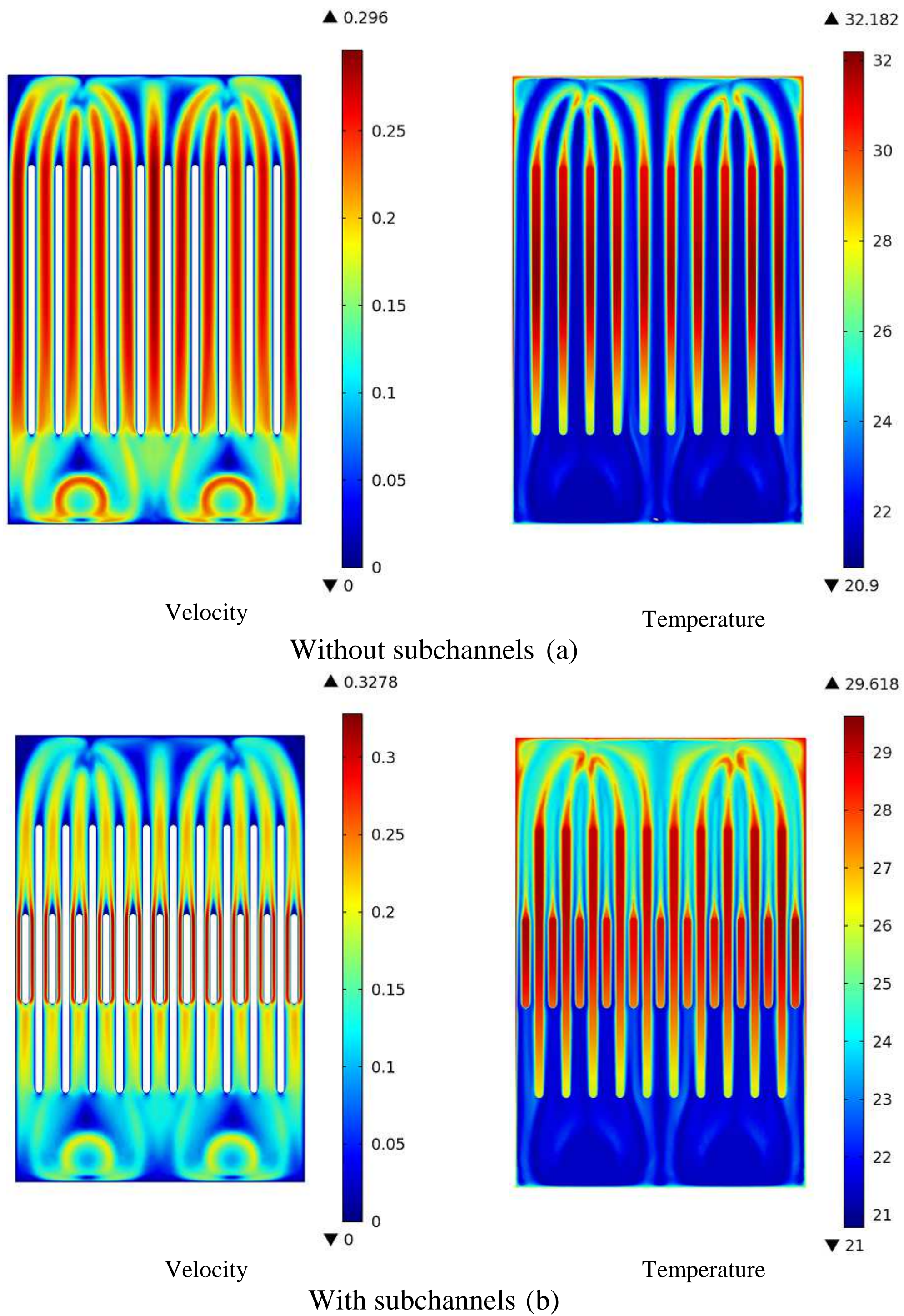

Fig. 14: Velocity and temperature distribution at the channels' middle height for the models: (a) without and (b) with subchannels.

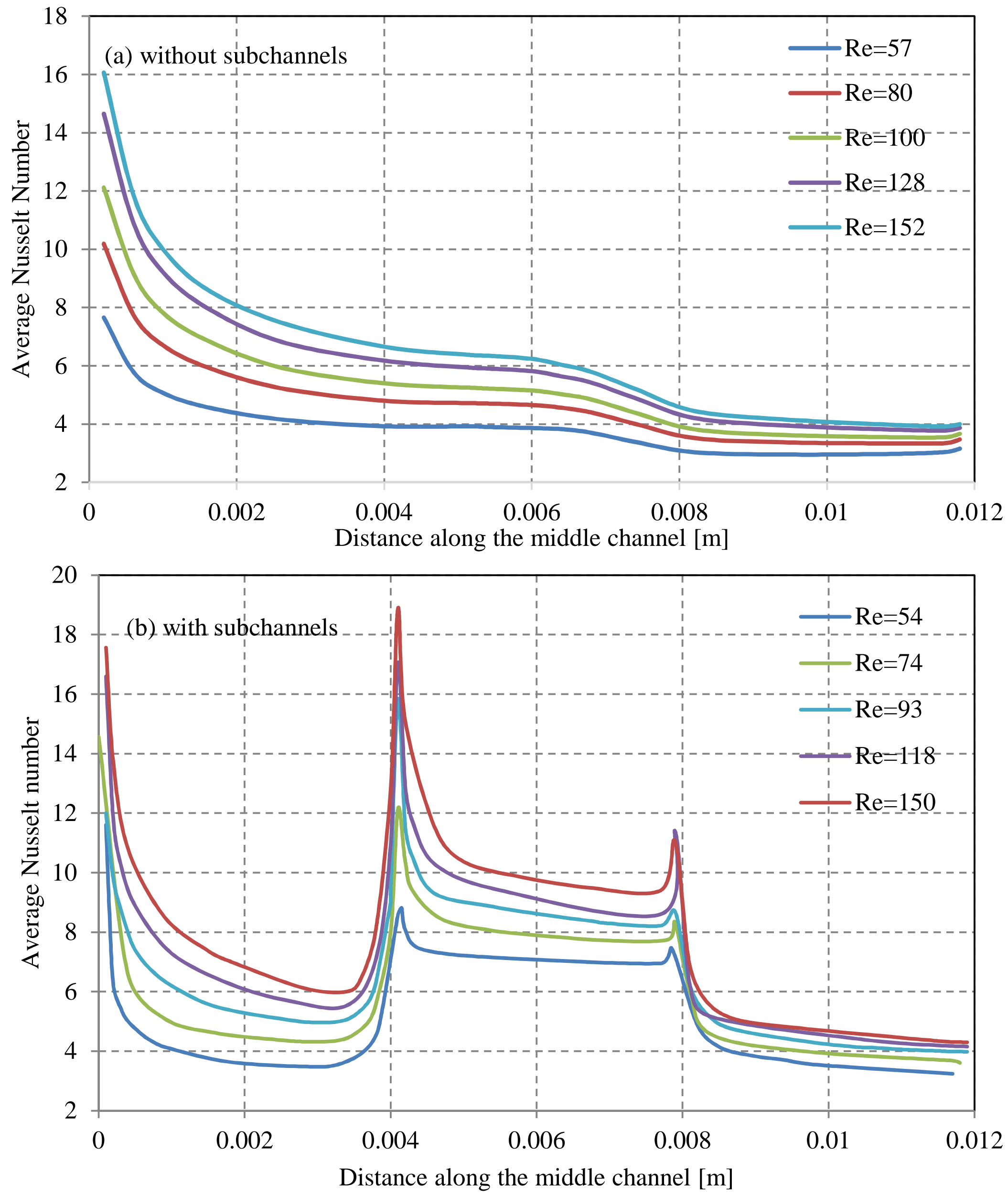

Fig. 15 Nusselt number variation along the middle channel for the models: (a) without and (b) with subchannels at different pressure heads.

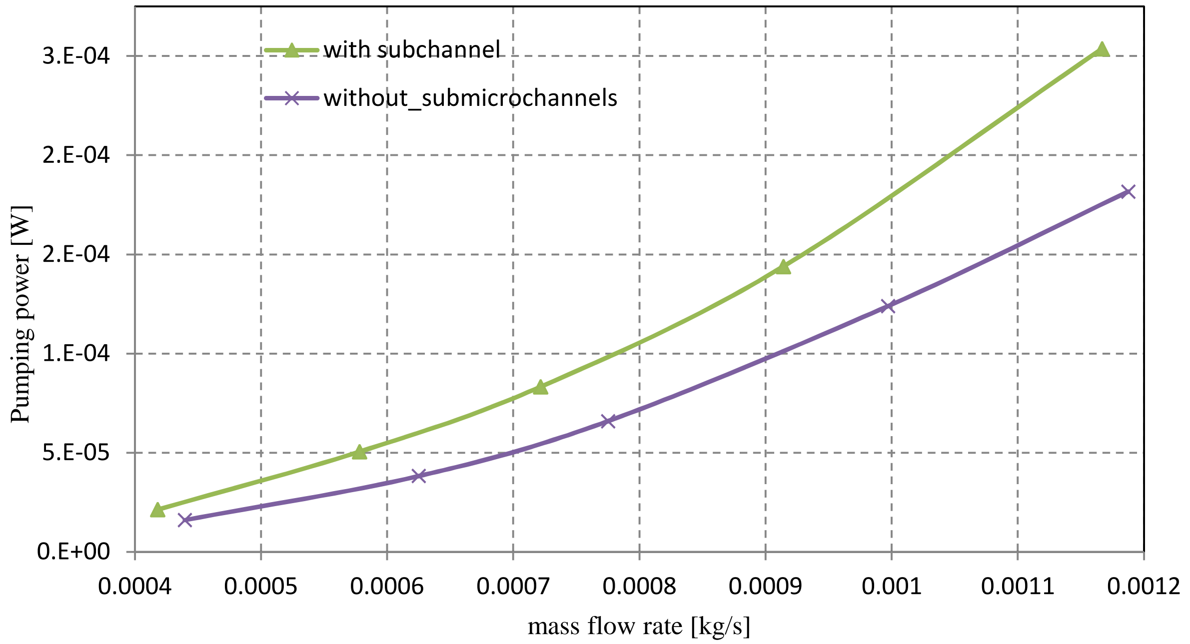

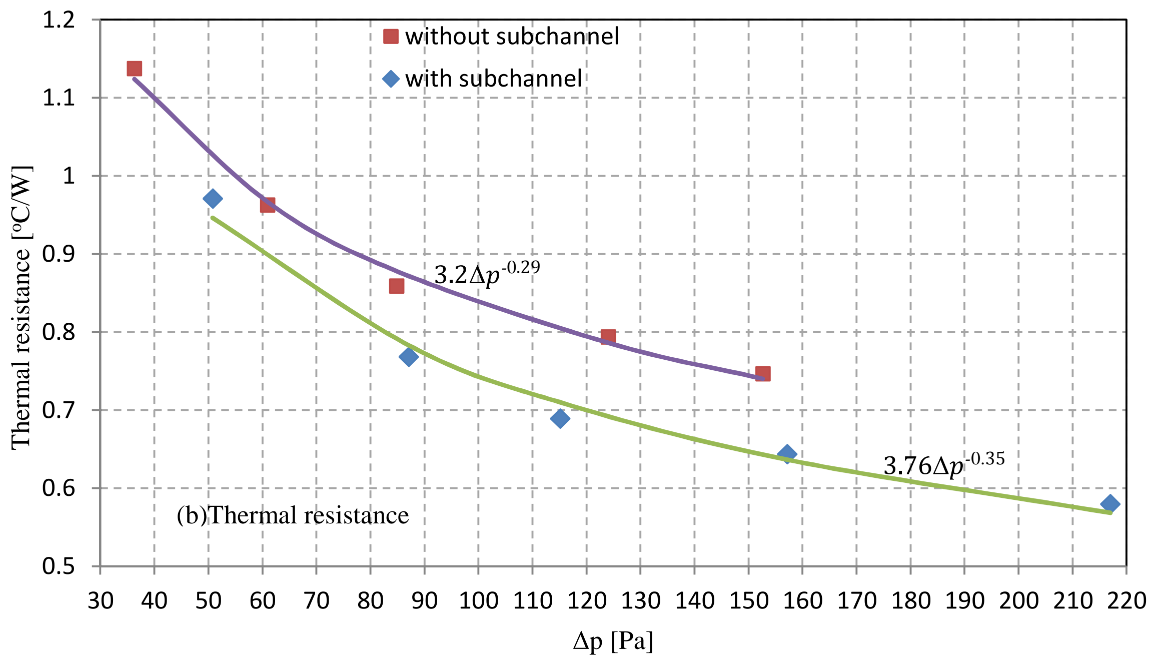

Fig. 16 Comparison between models without and with subchannels: (a) pumping power and (b) thermal resistance.

Table 1 Copper properties [40].

Density [kg/m^3]	8933
Specific heat capacity [J/kg K]	385
Thermal conductivity [W/m K]	401

Table 2 Average inlet velocity boundary conditions at different pressure heads.

	Without subchannels	With subchannels
Height [cm]	U_{uni} [m/s]	U_{uni} [m/s]
26	0.077	0.06
39	0.11	0.084
47	0.14	0.1
62	0.176	0.132
79	0.2	0.17

Table 3 Thermal inlet boundary conditions.

Inlet temperature [^{o}C]	21
Uniform heat flux [W/m^2]	4.45×10^4
Hotspot heat flux [W/m^2]	16.7×10^4

Nomenclature

Symbol	Definition
A	Cross-sectional area [m^2].
C_p	Specific heat capacity at constant pressure [J/kg K].
D_h=$2R$	Hydraulic diameter[m]=2*radius .
I	Current [A].
k	Thermal conductivity [W/m K].
L	Perimeter length [m].
$\dot{m}$	Mass flow rate [kg/s].
Nu	Nusselt number.
p	Pressure [Pa].
Δp	Pressure drop [Pa].
P	Electric power supply [W].
P_o	Pumping power [W].
$\dot{Q}$	Heat extracted by water [J/s]
q''	Average peripheral heat flux at a specific axial location [W/m^2].
Re	Reynolds number
R_{th}	Thermal resistance [$^oC/W$]
T	Temperature [K].
ΔT_{max}	$T_{s,max.} - T_{win}$ [K].
T_w	Temperature distribution along the wall's perimeter at a specific x-axis location [K].
u	Velocity component in the x-direction.
U	Velocity [m/s].
v	Velocity component in the y-direction.
V	Voltage [V].

μ	Kinetic viscosity [N s/m^2]
w	Velocity component in the z-direction.
ρ	Density [kg/m^3].
ν	Kinematic viscosity [m^2/s].
Subscript symbols	
$uniform$	Uniform flux surface.
$spot$	Hotspot heat flux.
w	Water
f	Fluid
b,avg	Average water bulk temperature [K].
inf	Environment.
s,max	Maximum surface temperature [K]
a,avg	Channel average temperature along the wall's perimeter at a specific location along the channel axis [K].
win	Water inlet temperature [K].
$wout$	Water outlet temperature [K].
avg	Average inlet velocity [m/s].
uni	Uniform inlet velocity [m/s].